Oriented ferromagnetic Fe-Pt alloy nanoparticles produced in Al_2O_3 by ion-beam synthesis

C. W. White[a)] and S. P. Withrow
Oak Ridge National Laboratory, Oak Ridge, Tennessee 37831

K. D. Sorge
The University of Tennessee, Knoxville, Tennessee 37996

A. Meldrum
The University of Alberta, Edmonton, T6G 2M7 Canada

J. D. Budai
Oak Ridge National Laboratory, Oak Ridge, Tennessee 37831

J. R. Thompson
The University of Tennessee, Knoxville, Tennessee 37996

L. A. Boatner
Oak Ridge National Laboratory, Oak Ridge, Tennessee 37831

(Received 11 September 2002; accepted 13 February 2003)

Oriented $Fe_{1-x}Pt_x$ nanoparticles have been formed in single-crystal Al_2O_3 host matrices by the sequential implantation of Fe and Pt ions followed by thermal annealing. For x in the range of ~35–55 at. % Pt, these nanoparticles are in the chemically ordered tetragonal $L1_0$ structure of FePt and appear to be fully ordered. The nanoparticles are ferromagnetic, and the magnetic coercivity is a strong function of the alloy composition, reaching values in excess of 20 kOe for $x \sim 45\%$. The crystallographic orientation and morphology of the nanoparticles are strongly dependent on the implantation conditions. Under certain implantation conditions, a buried amorphous layer can be formed in the Al_2O_3 matrix which crystallizes during annealing giving rise to the formation of an interconnected network of large FePt particles with a single orientation. Oriented nanoparticles of Fe_3Pt and $FePt_3$ were also synthesized. The Fe_3Pt and $FePt_3$ particles have the ordered, cubic $L1_2$ structure with an order parameter of 0.5–0.8; and these particles also exhibit ferromagnetic behavior. The magnetic and structural properties of the $Fe_{1-x}Pt_x$ nanoparticles are compared to and contrasted with those of nanoparticles of Fe and Pt in Al_2O_3 that were also formed by ion-beam synthesis. Evidence for Al incorporation into the nanoparticles is also presented. © *2003 American Institute of Physics.* [DOI: 10.1063/1.1565691]

I. INTRODUCTION

Materials with a high magnetocrystalline anisotropy and a high magnetization have generated considerable interest recently because they are excellent candidates for ultrahigh-density magnetic data storage applications.[1] These properties are required in order to maintain thermal stability when the bit size is reduced. FePt ordered alloys are in the class of materials known[2] to have a very large uniaxial magnetocrystalline anisotropy ($K_u \sim 7\times10^6$ J/m^3), and they have been the subject of considerable recent research. FePt alloys can exist either in a chemically disordered phase or as an ordered alloy in the CuAu family. In the chemically disordered structure, these materials have a face-centered cubic (fcc) unit cell in which the Fe and Pt atoms are distributed randomly on the lattice sites. As an ordered alloy, they have the face-centered tetragonal (fct) $L1_0$ structure, which consists of alternating planes of Fe atoms and Pt atoms stacked along the [001] direction of the crystal. It is this structure that gives rise to the very high magnetocrystalline anisotropy and, in turn, the high magnetic coercivity. Nanoparticles of FePt have previously been synthesized chemically as a superlattice of monodispersed spherical particles,[3] and films of $Fe_{1-x}Pt_x$ (with $x \sim 50\%$) with a high magnetic anisotropy have been prepared by a number of techniques including molecular beam epitaxy (MBE),[4] cosputtering,[5] sputtering of Fe/Pt multilayers,[6] and subsequent He-ion irradiation of Fe/Pt films deposited at low temperature.[7] Nanoparticles of $Fe_{1-x}Pt_x$ (with $x \sim 50\%$) have also been incorporated into matrices of amorphous Al_2O_3,[8,9] SiO_2,[10] Be_2O_3,[11] and Si_3N_4.[12]

In the present work, the sequential implantation of Fe and Pt ions into crystalline Al_2O_3 followed by thermal annealing was used to synthesize $Fe_{1-x}Pt_x$ nanoparticles that are encapsulated in the near-surface region of Al_2O_3 single crystals. These nanoparticles are crystallographically oriented with respect to the Al_2O_3 matrix, and both the orientation and microstructure depend significantly on the implantation conditions (such as substrate temperature). By varying the relative Fe and Pt doses, the Pt concentration in the alloy can be altered over a wide range. We find that the chemically

[a)]Electronic mail: whitecw@solid.ssd.ornl.gov

 © 2003 American Institute of Physics

Downloaded 11 Sep 2009 to 160.91.157.167. Redistribution subject to AIP license or copyright; see http://jap.aip.org/jap/copyright.jsp

ordered, $L1_0$ structure of FePt is formed over a range of Pt concentrations extending from ~35% to 55%, and the nanoparticles appear to be fully ordered. In this range, the $Fe_{1-x}Pt_x$ nanoparticles are ferromagnetic, and the magnetic coercivity is very high, reaching a value in excess of 20 kOe at 5 K for a Pt atomic fraction of ~45% in the alloy. By similar methods, samples with Pt atomic fractions of ~25% and ~75% were also produced and were found to contain oriented nanoparticles with the $L1_2$ structure expected for Fe_3Pt and $FePt_3$ respectively. Their magnetic properties are significantly different from those measured for samples where the Pt atomic fraction is nearly 50%. Finally, we discuss briefly the microstructure and magnetic properties of Fe and Pt nanoparticles formed in Al_2O_3 by the implantation of Fe or Pt alone. A preliminary account of some of this work can be found in Ref. 13.

II. EXPERIMENTAL PROCEDURE

Single crystals of Al_2O_3 (*c*-axis oriented unless otherwise stated) were used as substrates. These substrates were implanted by Fe ions (350 keV) and Pt ions (910 keV) to give overlapping concentration profiles of Fe and Pt with a projected range of ~175 nm for each element. The substrate was misoriented by a few degrees during implantation to minimize channeling effects. The samples were implanted with either 1×10^{17} or 5×10^{16} Fe/cm^2 and then with a Pt dose chosen to give the desired Pt atomic fraction x [where x = Pt dose/(Fe dose + Pt dose)] in the alloy (assuming complete alloying of the implanted species). Specimens were prepared with x in the range of 25–75 % as measured by Rutherford backscattering (RBS), which should be accurate to better than 1%. A few samples were implanted with Fe or with Pt alone in order to compare the results with those obtained for the FePt alloy samples. Implantation was carried out at elevated temperatures to reduce damage accumulation in an attempt to maintain crystallinity in the near surface of Al_2O_3 during implantation. In this work, samples were implanted either at high temperature (550 °C for Fe and 500 °C for Pt) or at somewhat lower temperature (200 °C for both Fe and Pt). The high temperature was sufficient to maintain crystallinity in the near surface of Al_2O_3 for the maximum doses used in this work ($\sim2\times10^{17}$/cm^2), but increased damage accumulation at the lower implant temperature (200 °C) led to the formation of a buried amorphous layer in the Al_2O_3 matrix (for doses of $\sim2\times10^{17}$/cm^2). The formation of this amorphous layer has a profound effect on the FePt orientation, microstructure, and particle size as will be discussed. Following the implantation, the samples were annealed in order to remove damage and to induce precipitation and nanocrystal formation. Annealing was carried out at 1100 °C for 2 h in a reducing environment (flowing Ar + 4% H_2) followed by slow cooling to near room temperature. The resulting specimens were characterized by RBS ion channeling measurements using 2.3 MeV He^+ ions, by x-ray diffraction (Cu $K\alpha$ radiation using both four-circle and powder diffractometers), and by cross-section transmission electron microscopy (TEM). The magnetic properties were measured using a superconducting quantum interference device (SQUID) magnetometer at temperatures between 5 and 400 K in applied magnetic fields up to ±65 kOe.

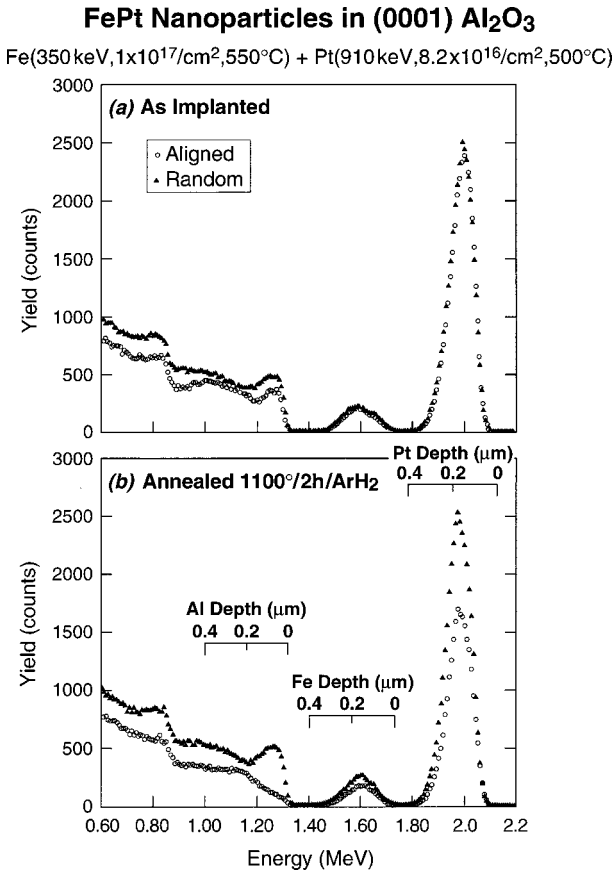

FIG. 1. RBS channeling measurements in the as-implanted state (a) and after annealing (b) for α-Al_2O_3 implanted by Fe (350 keV, 1×10^{17}/cm^2, 550 °C) and Pt (910 keV, 8.2×10^{16}/cm^2, 500 °C) followed by annealing (1100 °C/2 h/Ar+4%H_2). Depth scales appropriate for Pt, Fe, and Al in Al_2O_3 are indicated.

III. RESULTS

A. FePt Nanoparticles formed by high temperature implantation

Figure 1 shows the RBS channeling results for a sample implanted at high temperature with nearly equal doses of Fe and Pt. Backscattering spectra acquired with the He^+ ion beam aligned along the Al_2O_3 [0001] direction and with the beam incident along a random direction are shown for both the as-implanted state and after annealing. In the as-implanted state [Fig. 1(a)], the aligned spectra approaches but does not reach the random value in the Al portion of the spectrum, showing that the near surface of Al_2O_3 was heavily damaged—but not rendered amorphous by the ion implantation. Annealing removes a significant amount of the Al_2O_3 lattice damage and this results in significant ion channeling in both the Fe and Pt portions of the spectrum [Fig. 1(b)]. In addition, there is no redistribution in depth of the implanted impurities during annealing for samples implanted at these high temperatures. Assuming that complete alloying

Downloaded 11 Sep 2009 to 160.91.157.167. Redistribution subject to AIP license or copyright; see http://jap.aip.org/jap/copyright.jsp

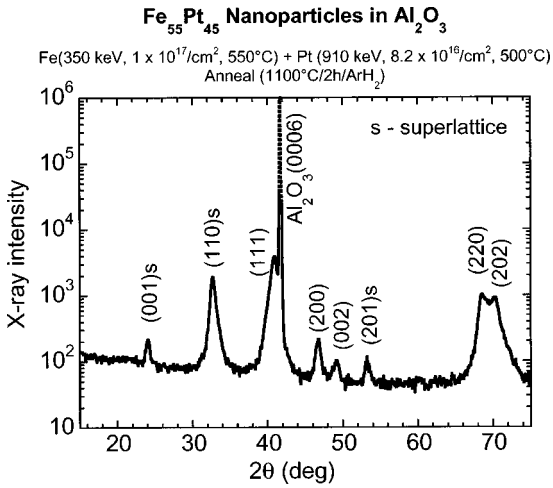

FIG. 2. X-ray diffraction results for *c*-axis-oriented Al_2O_3 implanted by Fe (350 keV, $1\times10^{17}/cm^2$, 550 °C)+Pt (910 keV, $8.2\times10^{16}/cm^2$, 500 °C) followed by annealing (1100 °C/2 h/Ar +4% H_2).

of the implanted species occurs during annealing, the Pt atomic fraction would be $x=45\%$, and the alloy formed would be $Fe_{55}Pt_{45}$.

Figure 2 shows the x-ray spectra for the FePt alloy formed in Al_2O_3 under the implantation and annealing conditions used for the sample of Fig. 1. In the as-implanted state, the only diffraction lines observed are from the Al_2O_3 substrate (pattern not shown). Following annealing, the θ-2θ scan along the *c*-axis of Al_2O_3 shows the expected strong (0006) diffraction line from Al_2O_3. All other diffraction lines in Fig. 2 arise from FePt; these lines are consistent with those expected from the $L1_0$ phase of FePt. Rocking-curve x-ray results (not shown) demonstrate that the FePt nanoparticles are oriented with respect to the *c*-axis of Al_2O_3, but from the results depicted in Fig. 2, there are multiple orientations for the nanoparticles [i.e., FePt (001), (110), (111), and several other orientations parallel to Al_2O_3 (0001)]. From the rocking-curve scans, the mosaic spread of the oriented nanoparticles is determined to be ~1.4°, consistent with the observation of channeling in the Fe and Pt parts of the spectrum in Fig. 1. In Fig. 2, there are three superlattice reflections (denoted by *s*) due to chemical ordering as well as several fundamental (fcc allowed) reflections from fct FePt. The existence of these superlattice reflections demonstrates that at least some of the nanoparticles are chemically ordered with the $L1_0$ structure. Determination of the tetragonal distortion of the FePt nanoparticles, as measured by the c/a ratio using the θ-2θ scan of Fig. 2, is complicated by the fact that the peaks arise from different grains. Nevertheless, we can use reflections from different grains to indirectly estimate *c* and *a* for these nanoparticles. From the (200) reflection, a value for *a* of ~3.886 Å is determined; and from the (002) reflection, a value for *c* of ~3.704 Å is determined. Consequently, the tetragonal distortion of the FePt nanoparticles of Fig. 2(a) is estimated to be ~0.95 in reasonable agreement with the value of 0.96 expected[2] for bulk equiatomic FePt.

TABLE I. Calculated intensity ratios for fully ordered FePt thin films with domains oriented normal to the surface. Results are shown for stoichiometric FePt, for nonstoichiometric FePt ($Fe_{55}Pt_{45}$), and for the stoichiometric case with 20% Al on the Fe sites. Results are also shown for Fe_3Pt and $FePt_3$ with the cubic $L1_2$ structure. Intensity ratios for both (002) and (220) domains are given.

Composition	Structure	$I(001)/I(002)$	$I(110)/I(220)$
FePt	$L1_0$	1.56	1.95
$Fe_{55}Pt_{45}$	$L1_0$	1.41	1.77
$Fe_{40}Al_{20}Pt_{40}$	$L1_0$	1.77	2.19
Fe_3Pt	$L1_2$	0.72	0.95
$FePt_3$	$L1_2$	0.23	0.30

The *d* spacings can be inferred from high-resolution x-ray scans of the strong diffraction lines in Fig. 2. For example, the *d* spacing for the (111)-oriented nanoparticles is ~2.204 Å, and for the (110)-oriented nanoparticles it is ~2.735 Å—compared to 2.197 and 2.725 Å for bulk FePt. These measurements imply an expansion of ~0.35% compared to the bulk values.[14] Such an expansion might result from lattice matching to the Al_2O_3 host, to a deviation of 5% from equiatomic stoichiometry, or to the incorporation of displaced Al into the nanoparticles during precipitation.

An estimate of how well ordered the alloy is can be obtained by determining the one-dimensional chemical ordering parameter *S* defined[15–17] as

$$S=(r_{Fe}-x_{Fe})/y_{Pt}=(r_{Pt}-x_{Pt})/y_{Fe}, \tag{1}$$

where $r_{Fe(Pt)}$ is the fraction of Fe (Pt) sites occupied by the correct atomic species, $x_{Fe(Pt)}$ is the atomic fraction of Fe (Pt) in the sample (1/2 for equiatomic stoichiometry), and $y_{Fe(Pt)}$ is the fraction of Fe (Pt) sites (1/2 for equiatomic stoichiometry). The fraction (w_{Fe}) of Fe sites occupied by Pt (i.e., the "wrong" atom) is

$$w_{Fe}=1-r_{Fe} \tag{2}$$

and for a perfectly ordered FePt crystal $S=1$ and $r_{Fe}=1$. A perfectly disordered crystal has $S=0$, $r_{Fe}=1/2$, and $w_{Fe}=1/2$.

Experimentally, the chemical order parameter can be determined by measuring the intensity ratios of the superlattice to fundamental reflections and comparing these ratios to calculated values in the following manner:

$$S^2=\frac{[I_s/I_f]_{measured}}{[I_s/I_f]_{calculated}}. \tag{3}$$

Here, I_s and I_f are the integrated intensities of the superlattice peak and the corresponding fundamental x-ray diffraction peak, respectively, and the calculated ratio assumes a perfectly ordered alloy. Calculated intensities of both fundamental and superlattice reflections can be obtained using known atomic fractions, atomic scattering factors, Debye-Waller factors, Lorenz polarization factors, and structure factors (a general discussion of the procedure to calculate intensities is found in Ref. 15, Chapter 4). From these estimates, the calculated intensity ratios for thin films (assuming perfect order with domains oriented normal to the surface) are shown in Table I for stoichiometric FePt and nonstoichiomet-

Downloaded 11 Sep 2009 to 160.91.157.167. Redistribution subject to AIP license or copyright; see http://jap.aip.org/jap/copyright.jsp

ric $Fe_{55}Pt_{45}$ with the $L1_0$ structure. (Table I also shows the calculated intensity ratios for cubic Fe_3Pt and $FePt_3$ with the $L1_2$ structure.)

For the sample of Fig. 2, the integrated intensity ratio of superlattice to fundamental reflections $I(001)/I(002)$ was measured to be ~1.85 (±0.15) from rocking-curve measurements. This value is larger than the predicted intensity ratio for either fully ordered FePt or $Fe_{55}Pt_{45}$ (Table I). This would suggest that the order parameter S is greater than unity [Eq. (3)]—a result with no physical meaning. Consequently, a structural modification other than site disorder and/or Fe/Pt stoichiometry is contributing to the measured intensity ratio. A likely possibility is that lighter Al atoms from the substrate are incorporated into the FePt precipitates. Since the structure factor F_{hkl} depends directly on the difference in the atomic scattering factors of the Fe and Pt sites, substituting Al atoms onto the Fe site will yield more intense superlattice peaks. As shown in Table I, if the fully ordered alloy contains 20% Al, then the predicted intensity ratio is increased and becomes comparable to that which is measured. This is strong (although indirect) evidence that the FePt alloys produced by ion-beam synthesis are fully ordered and contain Al atoms in addition. Further evidence for the hypothesis that the nanoparticles contain Al is given by the observation that ordered alloy nanoparticles of the form Pt_nAl are produced under certain conditions by the implantation of Pt alone into Al_2O_3 followed by thermal annealing (to be discussed later). Accordingly, under the redox conditions employed in the high-temperature annealing process utilized here, and given the low oxygen affinity of Pt, the incorporation of some Al into the FePt alloy nanoparticles would not be surprising. Consequently, the FePt nanoparticles shown in Fig. 2 appear to be fully ordered and most likely also contain Al atoms. Note that since the degree of chemical order and Al substitutions both influence the superlattice-to-fundamental intensity ratios, we cannot independently quantify these two effects from x-ray measurements.

The above discussion considered the (001)-oriented FePt precipitates in Fig. 2. For the (220)-oriented domains, the close proximity of the (220) and (202) reflections precludes the use of sufficiently wide detector slits to accurately determine the integrated intensity ratio $I(110)/I(220)$. Instead, the areas of these reflections, as deconvoluted from the θ-2θ scan in Fig. 2, were used to estimate the intensity ratio. For the (220)-oriented domains, the measured intensity ratio $I(110)/I(220)$ is ~1.34 ±0.14 compared to a value of ~1.77 for a fully ordered $Fe_{55}Pt_{45}$ alloy. This implies an order parameter of $S \sim 0.87$ for these domains. This is only an estimate since rocking curves could not be used for integrated intensity measurements.

The strongest FePt reflection in the θ-2θ scans of Fig. 2 is the FePt (111) peak. For these (111)-oriented domains, there is no superlattice reflection with which to compare intensities in a scan along the surface normal. In principle, off-axis scans (at ~36.5° from the normal) through the (110) and (220) reflections for the (111)-oriented domains could be used to obtain the intensity ratios necessary to determine the order parameters for the (111)-oriented domains. Such scans were attempted, but this sample contains multiple domains, and it was not possible to obtain a clean separation of the reflections necessary to determine accurate integrated-intensity measurements for the (111) domains. Nevertheless, based on the intensity estimates from off-axis θ-2θ scans, it appears that the (111) domains are also highly ordered. Therefore, the x-ray diffraction results are consistent with well-ordered grains for the FePt nanoparticles in this sample, and the measurements for the (001)-oriented nanoparticles suggest that the Al atoms are incorporated on Fe sites.

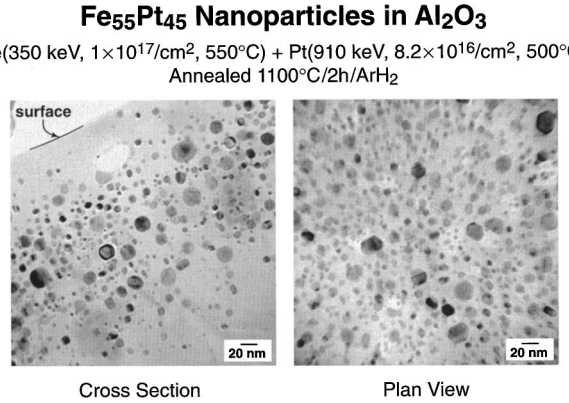

FIG. 3. Cross-section and plan-view TEM micrographs for the sample of Figs. 1 and 2.

The microstructure in the near-surface region for the sample of Figs. 1 and 2 is shown by the cross-section and plan-view TEM micrographs given in Fig. 3. Most of the FePt nanoparticles are in the size range of 2–10 nm in diameter with a few nanoparticles as large as 20 nm in diameter. Evidence for faceting is also observed in some of the nanoparticles in Fig. 3 particularly in the plan-view images. High-resolution θ-2θ x-ray scans across the (111) diffraction line give a coherence length normal to the surface of ~13 nm for (111)-oriented nanoparticles—consistent with the TEM determinations of the particle size.

Magnetic properties of the encapsulated $Fe_{1-x}Pt_x$ nanoparticles were determined using a SQUID magnetometer. Figure 4 shows the raw data obtained using the SQUID for the sample of Figs. 1–3. In this figure, the magnetic moment of the sample (in units of Bohr magnetons per implanted ion)

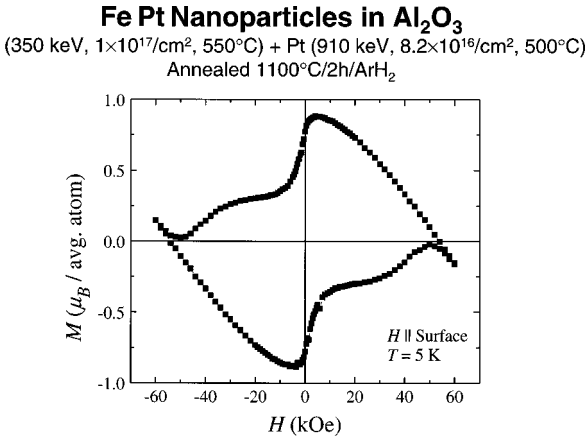

FIG. 4. SQUID measurements of the magnetic moment of the implanted sample of Figs. 1–3.

Downloaded 11 Sep 2009 to 160.91.157.167. Redistribution subject to AIP license or copyright; see http://jap.aip.org/jap/copyright.jsp

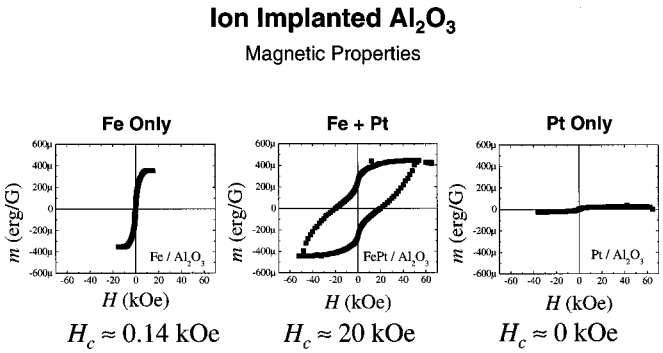

FIG. 5. Magnetization measurements (made at $T=5$ K with H normal to the surface) for Al_2O_3 crystals implanted by Fe only (350 keV, $1\times10^{17}/cm^2$), by Pt only (910 keV, $8.2\times10^{16}/cm^2$) and by Fe (350 keV, $1\times10^{17}/cm^2$) + Pt (910 keV, $8.2\times10^{16}/cm^2$). Implantation was carried out at 550 °C for Fe and 500 °C for Pt. Implanted samples were annealed (1100 °C/2 h/Ar + 4% H_2).

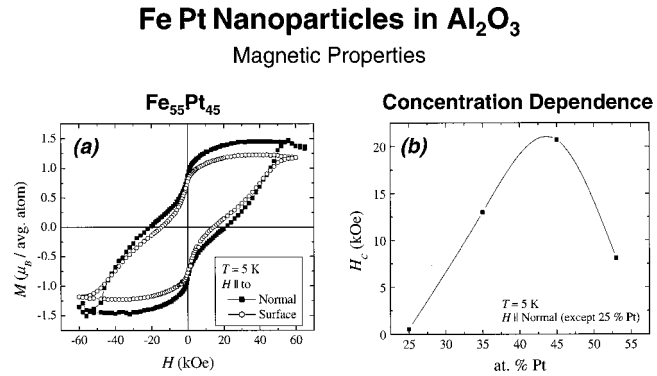

FIG. 6. Magnetic properties of $Fe_{1-x}Pt_x$ nanoparticles in Al_2O_3. Magnetization curves for $Fe_{55}Pt_{45}$ are shown in (a) for two different field orientations at $T=5$ K. The dependence of H_c on alloy composition is shown in (b). All samples were implanted by Fe at 550 °C and Pt at 500 °C. In (b), all measurements were made at $T=5$ K with H normal to the surface except for the sample with 25% Pt, where the applied magnetic field was parallel to the surface.

is measured at $T=5$ K as the magnetic field is scanned in the range of ±65 kOe. Al_2O_3 is diamagnetic, and this accounts for the negative slope in the magnetization curves at very high fields. (For the subsequent SQUID data presented in this paper, the diamagnetic signal from Al_2O_3 have been subtracted.) The hysteresis in Fig. 4 reflects the ferromagnetic nature of the FePt nanoparticles. The magnetic coercivity is in excess of 20 kOe for the FePt nanoparticles—as is more clearly evident in the background-corrected data presented in Fig. 5(b).

The high magnetic coercivity of the FePt nanoparticles as shown in Fig. 4 results from the alloying of Fe and Pt. This is demonstrated in Fig. 5 where the magnetization results are shown for samples implanted by Fe only, by Pt only, or by Fe+Pt with the alloy composition $Fe_{55}Pt_{45}$. For the case of Fe implantation only, the coercive field is rather low, only ~0.14 kOe (at $T=5$ K). Here the saturation moment corresponds to $\sim2.4\mu_B$ (Bohr magnetons) per Fe atom, which is comparable with the value ($2.2\mu_B$) for bulk bcc iron. For the case of Pt only, both the saturation moment and the coercive field are nearly zero as expected. In the case of thermally processed $Fe_{55}Pt_{45}$ alloy sample however, the coercive field is very large, greater than 20 kOe. This high coercivity arises from FePt nanoparticles in the fct $L1_0$ structure. For this material, the saturation signal corresponds to a mean atomic moment of $1.5\mu_B$ per atom of alloy, i.e., the macroscopic magnetic moment divided by the total number of (Fe+Pt) atoms. This result lies between the values reported for bulk samples of FePt with this composition, in disordered ($1.65\mu_B$) and ordered states ($\geqslant1.15\mu_B$);[18] the latter value, however, is considered to be a lower bound, due to difficulties in saturating the hysteretic ferromagnetic in the available field[18] and the necessity to extrapolate the measurements from 77 K to low temperatures.

Magnetization measurements for the $Fe_{55}Pt_{45}$ nanoparticles formed in Al_2O_3 are shown in Fig. 6(a) for two different magnetic field orientations. The coercive field is ~22 kOe with the applied field oriented normal to the sample surface, and it is ~15 kOe with the field parallel to the surface. These values of coercivity may represent lower limits since the magnetization may not be fully saturated even at an applied field of 65 kOe. The magnetization measurements are similar since very few of the nanoparticles are oriented with the "easy axis" of magnetization [001] normal to the surface. For both field orientations, the hysteresis loops are not square, and there is an obvious second set of shoulders at $H=0$. Features similar to this have been seen previously.[19–22] In the present work, it is not clear what causes these features to develop, but others[20] have reported similar hysteresis loops and have attributed their presence to the superposition of two hysteresis loops, one arising from a soft magnetic phase and the other arising from the hard magnetic $L1_0$ phase of FePt. In the work reported in Ref. 20, the soft magnetic material was attributed to small grains of a fcc phase embedded in larger grains of the ordered $L1_0$ phase of FePt. The extra shoulders develop when there is little or no exchange coupling between the magnetically hard and soft phases.[20] In our case, the soft phase might be the disordered fcc phase of FePt or possibly small quantities of Fe_3Pt or $FePt_3$. We cannot exclude these phases being present at low concentrations, but there is no evidence in the x-ray diffraction results for their presence. Other possible causes include antiferromagnetic coupling[23] or effects related to a nonuniform (bimodal) size distribution of the nanoparticles. Further work is currently in progress to clarify the origin of these features.

The Pt concentration in the alloy can be changed over a wide range by altering the relative doses of Fe and Pt during ion implantation. Figure 6(b) shows the variation of magnetic coercivity with the Pt atomic fraction. For these measurements, the Fe dose was fixed at $1\times10^{17}/cm^2$, and the Pt dose was changed to produce the desired alloy composition, assuming complete alloying of the implanted species. In Fig. 6(b), the coercivity is a strong function of alloy composition reaching a maximum value of ~22 kOe for a Pt atomic fraction of ~45% and then falling rapidly on either side. At a Pt concentration of ~25%, the coercive field is nearly zero, but x-ray diffraction measurements from this sample (discussed later) are consistent with those expected from Fe_3Pt, which

Downloaded 11 Sep 2009 to 160.91.157.167. Redistribution subject to AIP license or copyright; see http://jap.aip.org/jap/copyright.jsp

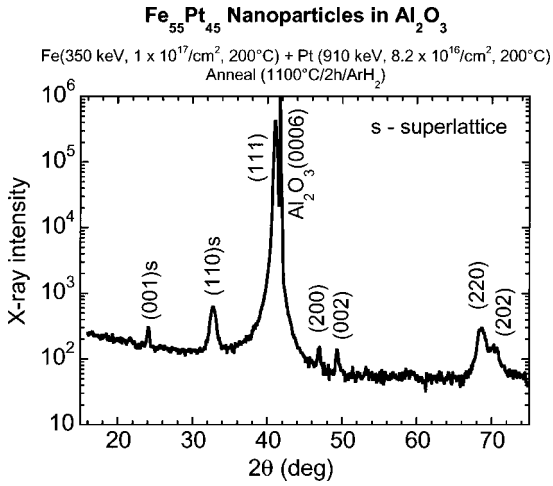

FIG. 7. X-ray diffraction results for *c*-axis-oriented Al_2O_3 implanted by Fe (350 keV, $1\times10^{17}/cm^2$)+Pt (910 keV, $8.2\times10^{16}/cm^2$) at 200 °C and then annealed (1100 °C/2 h/Ar+4% H_2).

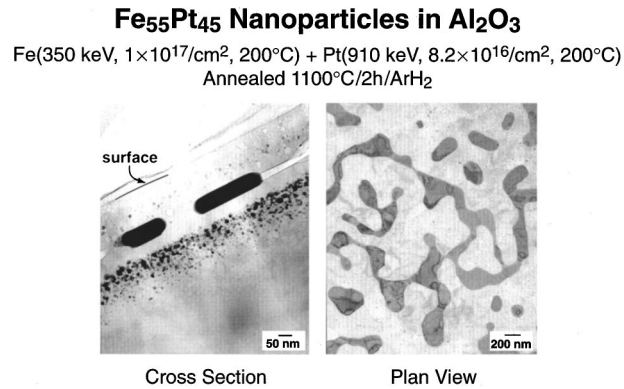

FIG. 8. Cross-section (left) and plan-view (right) TEM results for *c*-axis-oriented Al_2O_3 implanted by Fe (350 keV, 1×1017/cm2)+Pt (910 keV, $8.2\times10^{16}/cm^2$) at 200 °C followed by annealing (1100 °C/2 h/Ar +4% H_2).

is also an ordered alloy but with the cubic $L1_2$ structure. The other samples treated in Fig. 6(b) have x-ray spectra characteristic of the fct $L1_0$ phase of FePt. The dependence of H_c on Pt concentration shown in Fig. 6(b) is similar to that reported by others,[3] but the coercive fields in Fig. 6(b) are considerably higher than those reported in Refs. 3–12. With one exception,[22] the coercivities determined in this work are comparable to the highest reported for FePt alloys formed by any method.[20,24] It is possible that the increased coercivity in this work might result from the incorporation of Al into the ordered alloy nanoparticles. Others have observed significant reductions in the structural ordering temperature for FePt (Ref. 25) and for CoPt (Ref. 26) caused by the incorporation of various impurities, and it has also been shown that the addition of boron to FePt alloys will increase the coercivity.[2]

B. FePt nanoparticles formed by implantation at 200 °C

Reducing the implantation temperature to 200 °C leads to enhanced damage accumulation during implantation, which results in the formation of a buried amorphous layer in the Al_2O_3 matrix for the highest doses used in this experiment. This has a dramatic effect on the FePt orientation, microstructure, and particle size compared with results obtained by high-temperature implantation to the same dose. Figure 7 illustrates x-ray diffraction results from a sample implanted to the same dose as that of Fig. 2, but in this case, the implantation temperature was 200 °C for both ion species. Following annealing, the θ-2θ scan along the *c*-axis of Al_2O_3 shows a very intense (111) FePt diffraction line, and all other lines from FePt are down in intensity by nearly three orders of magnitude. Therefore, under these implantation and annealing conditions, almost all of the nanoparticles are oriented with their [111] axis parallel to the *c*-axis of Al_2O_3. This is in marked contrast to the results achieved by implantation at the higher temperature (see Fig. 2) where the x-ray intensities from several different orientations of nanoparticles are significant. From high-resolution scans, we infer a $d(111)$ lattice spacing of 2.198 Å which is very close to the bulk value for fct FePt. Consequently, a single orientation of nanoparticles has been achieved by the implantation/annealing conditions of Fig. 7—whereas a multiple orientation of nanoparticles results from the implantation/annealing conditions of Fig. 2. The nanoparticles resulting from the 200 °C implantation also exhibit a strong in-plane alignment. The in-plane orientation for the FePt nanoparticles is $FePt(11\bar{2})\parallel\alpha\text{-}Al_2O_3(11\bar{2}0)$ and 60° rotations.

The structure of the FePt nanoparticles of Fig. 7 is slightly distorted from the expected tetragonal $L1_0$ structure. For bulk FePt, Ref. 14 gives values of $a=b=3.8525$ Å, $c=3.7133$ Å, $\alpha=\beta=\gamma=90°$, for a tetragonal distortion (c/a ratio) of 0.964. Using high-resolution scans to measure the positions of the FePt lines in Fig. 7, we find these peaks are consistent with $a=b=3.878$ Å, $c=3.698$ Å, $\alpha=\beta=90.07°$, $\gamma=90.28°$ for a tetragonal distortion (c/a ratio) of 0.954.

In the scans made at 36.5° from the normal for this sample, the integrated intensity ratio $I(110)/I(220)$ for the (111)-oriented nanoparticles is 2.22 ± 0.12 which is larger than that predicted for fully ordered FePt or $Fe_{55}Pt_{45}$ as shown in Table I. (The results given in Table I are for scans along the surface normal, but the results for off-axis scans at 36.5° differ from these values by less than 1%.) If ~20% Al is incorporated into the alloy, then the predicted intensity ratio increases and is comparable to the experimentally measured values (Table I). This is strong evidence that the FePt nanoparticles in this sample are fully ordered but also may contain ~20% of incorporated Al.

The microstructure and particle size are also dramatically different in the sample implanted at 200 °C as demonstrated by the cross-section and plan-view TEM results shown in Fig. 8. In cross section, the large FePt nanoparticles are ~50 nm thick, in good agreement with a coherence length of 45 nm determined from high-resolution x-ray diffraction θ-2θ scans. These large particles are parallel to the surface and centered at a depth of ~150 nm. Below this depth, there is a band of very small particles. The large particles in the cross-section micrograph of Fig. 8 have dimensions of ~300 nm, parallel to the surface, which is much larger than the nanoparticles resulting from the high-

Downloaded 11 Sep 2009 to 160.91.157.167. Redistribution subject to AIP license or copyright; see http://jap.aip.org/jap/copyright.jsp

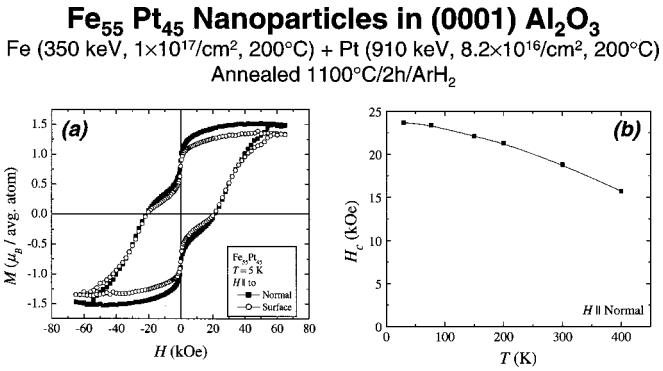

FIG. 9. Magnetic properties of the implanted sample of Figs. 7 and 8. Magnetization measurements (at $T=5$ K) are shown in (a) for two applied magnetic field orientations. The temperature dependence of the coercive field is shown in (b) with H oriented normal to the surface.

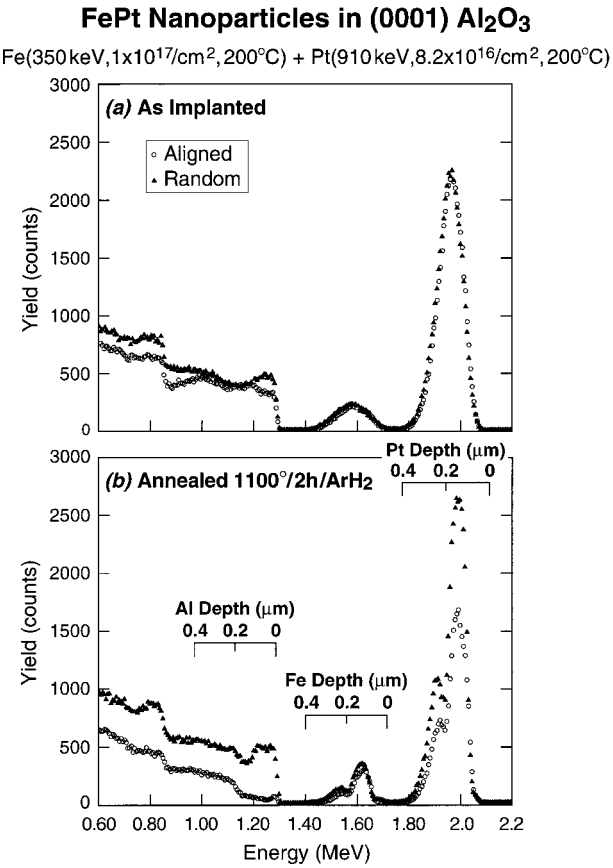

FIG. 10. RBS channeling measurements for c-axis-oriented Al_2O_3 implanted by Fe (350 keV, $1\times10^{17}/cm^2$, 200 °C)+Pt (910 keV, $8.2\times10^{16}/cm^2$, 200 °C). Measurements are shown in the as-implanted state (a) and after annealing (b).

temperature implantation (Fig. 3). The plan-view micrograph of Fig. 8 shows that the particles are even larger than the results suggested by the cross-section micrograph. In plan view, the FePt particles have a threading, wormlike shape that can extend for distances up to ~2 μm parallel to the surface. Thus, under these implantation and annealing conditions, the particles are interconnected and form a network of threading particles. The volume fraction of FePt in the network layer is quite high (25–30 %). A similar microstructure and particle size for FePt in Al_2O_3 has been produced by others[8,27] using simultaneous ion-beam sputtering of FePt and Al in the presence of oxygen. Much higher volume fractions of FePt were required, however, in order to obtain a similar microstructure, and there is no indication that the FePt nanoparticles were crystallographically oriented in that work.

Nanoparticles formed by implantation at 200 °C also have a high magnetic coercivity as demonstrated in Fig. 9. In Fig. 9(a), the coercive field deduced from both field orientations is ~23 kOe at 5 K. This is approximately the same coercive field as that determined for the sample implanted at much higher temperatures [see Fig. 6(a)] where the nanoparticle sizes are significantly smaller than those obtained by implantation at 200 °C (compare the particle size in Fig. 3 with that in Fig. 8). Figure 9(b) shows the temperature dependence of coercivity and demonstrates that the coercivity remains in excess of 15 kOe even at 400 K. The second set of shoulders that develop at $H=0$ in the magnetization curves of Fig. 9(a) is more pronounced than that in the magnetization curves shown in Fig. 6(a). This suggests that the exchange coupling between the hard and soft phases is not as strong in the 200 °C implantation case.

The synthesis of the unusually large particles shown in Fig. 8 appears to be related to the formation of a buried amorphous layer during implantation as suggested by the RBS channeling measurements in Fig. 10. In the as-implanted state [Fig. 10(a)], the channeling measurements in the Al sublattice show that the extreme near surface is crystalline after implantation, but below this outer surface, there is a buried amorphous layer extending from a depth of ~90 to ~300 nm. In this depth range, the aligned yield reaches the random value in the Al sublattice. Annealing [Fig. 10(b)] crystallizes the buried amorphous layer, accompanied by a redistribution of the implanted ions into two distinct bands at depths that correspond to the band of large particles and the band of very small particles seen in the cross-section micrograph of Fig. 8. From the results shown in Fig. 10, it is likely that crystallization of the buried amorphous layer occurred by a solid-phase epitaxial process in which the two amorphous/crystalline interfaces moved toward each other, accompanied by segregation of the impurities at the interface. This process could result in a thin layer of very high impurity concentration that gave rise to the interconnected network of large particles. It is likely that the large particles form from a coalescence of smaller particles, and at higher resolution there is evidence for grain boundaries as well as twinning in the large particles. Presumably, the large particles occur when the volume fraction of the metal phase exceeds the percolation threshold, and the increase of impurity concentration would be assisted by segregation of the impurities at the two moving interfaces during annealing.

Previous studies[28–30] have shown that, when a thin layer of crystalline α-Al_2O_3 is made amorphous by ion implantation, crystallization of the amorphous layer takes place by two epitaxial growth processes. Amorphous Al_2O_3 first crystallizes epitaxially into the metastable cubic γ phase of Al_2O_3 where the (111) γ is parallel to the (0001) α. Further annealing transforms the metastable γ phase back to the

Downloaded 11 Sep 2009 to 160.91.157.167. Redistribution subject to AIP license or copyright; see http://jap.aip.org/jap/copyright.jsp

stable α phase by a second solid-phase epitaxial growth process. It has been demonstrated[31] also that the size, structure, and orientation of semiconductor nanoparticles can (in some cases) be changed considerably by precipitation in the γ layer compared with precipitation in α-Al_2O_3. For the sample of Figs. 7 and 8, it is likely that precipitation and FePt nanocrystal formation took place in the γ phase of Al_2O_3 with the (111) FePt parallel to the (111) γ-Al_2O_3. When the γ phase subsequently transformed to the α phase, this would leave the (111) FePt parallel to the (0001) α-Al_2O_3. From the results presented in Figs. 2 and 7, it is clear that a single orientation of nanoparticles results during annealing when the implant creates a buried amorphous layer, whereas multiple orientations result when precipitation takes place in the crystalline α alumina phase. Precipitation and FePt nanoparticle formation in the metastable γ phase might account for this difference.

The formation of the network of large FePt particles can be prevented by carrying out the implantation in such a way that an amorphous layer does not form during implantation. One way to accomplish this is to implant at high temperatures so that the implanted region remains crystalline, as demonstrated by the results shown in Figs. 1–3. Another way to accomplish this is to implant at the lower temperature (200 °C) and keep the same alloy composition, but to reduce the total dose of each ion to avoid formation of the amorphous layer. Figure 11 shows the results obtained by implanting at 200 °C but reducing the dose of Fe and Pt by a factor of 2 compared with the doses used for the sample of Figs. 7–10. At this reduced dose, the overall alloy composition remains the same ($Fe_{55}Pt_{45}$), but the implanted region clearly remains crystalline during implantation [Fig. 11(a)]. Most of the damage is removed by annealing [Fig. 11(b)], and there is essentially no impurity redistribution during the annealing process. This behavior is very similar to that depicted in Fig. 1 for the higher-dose and higher-temperature implant.

Figure 12 shows x-ray diffraction and TEM results for the sample implanted at 200 °C with the lower ion dose. The x-ray spectrum shows evidence of FePt nanoparticles with several orientations [for example, (110) and (111)] and is qualitatively similar to the results of Fig. 2. The cross-section micrograph in Fig. 12(b) shows particles that are much smaller than those found in the sample implanted to the higher dose at 200 °C (Fig. 8). In Fig. 12(b), the maximum particle diameter is ~15 nm, and the microstructure is similar to that of Fig. 3 but the particle size is somewhat less than that of Fig. 3 which probably reflects the fact that the total ion dose is reduced by a factor of 2. Both the microstructure and the maximum particle size are dramatically different from the results of Fig. 8, even though the two samples are implanted and annealed at the same temperatures, but different ion doses were used.

The magnetic coercivity for the lower-dose sample is high, but it is reduced in comparison to that for the higher-dose samples. Magnetization measurements (at 5 and 300 K) for the sample implanted at 200 °C at the lower dose are shown in Fig. 13. The coercivity at 5 K is ~5.8 kOe and it is ~3.4 kOe at 300 K. These values of coercivity are considerably less than those for the samples implanted at the higher doses [Figs. 6(a) and 9(a)]. The reduction in coercivity compared with the results in the higher-dose samples may be related to the reduction in the particle size. In addition, the shape of the magnetization curve in Fig. 13 suggests that this sample has a larger fraction of the soft magnetic phase than

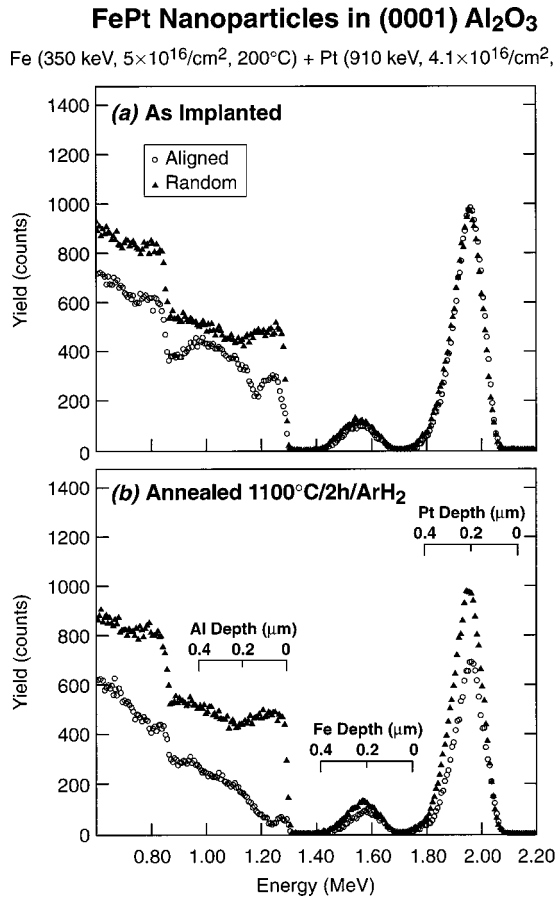

FIG. 11. RBS channeling measurements for *c*-axis-oriented Al_2O_3 implanted by Fe (350 keV, $5\times10^{16}/cm^2$, 200 °C)+Pt (910 keV, $4.1\times10^{16}/cm^2$, 200 °C). Measurements are shown in the as-implanted state (a) and after annealing (b). Ion doses are reduced by a factor of 2 compared with the sample of Fig. 10.

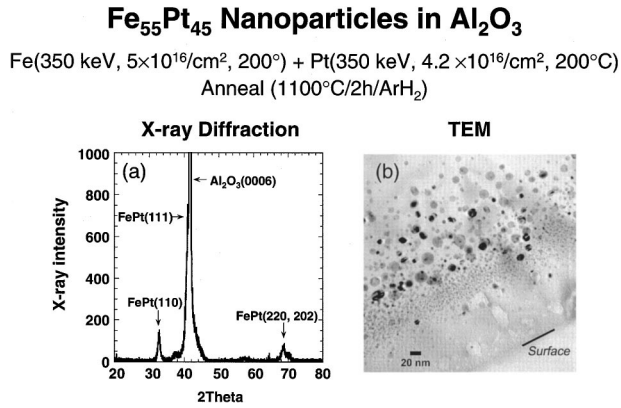

FIG. 12. X-ray diffraction (a) and cross-section TEM results (b) for *c*-axis-oriented Al_2O_3 implanted by Fe (350 keV, $5\times10^{16}/cm^2$, 200 °C) +Pt (910 keV, $4.1\times10^{16}/cm^2$, 200 °C) followed by annealing (1100 °C/2 h/Ar+4% H_2).

Downloaded 11 Sep 2009 to 160.91.157.167. Redistribution subject to AIP license or copyright; see http://jap.aip.org/jap/copyright.jsp

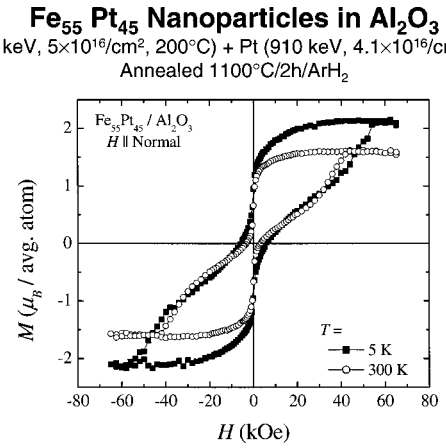

FIG. 13. Magnetization measurements (made at $T=5$ K and 300 K) for the sample of Fig. 12.

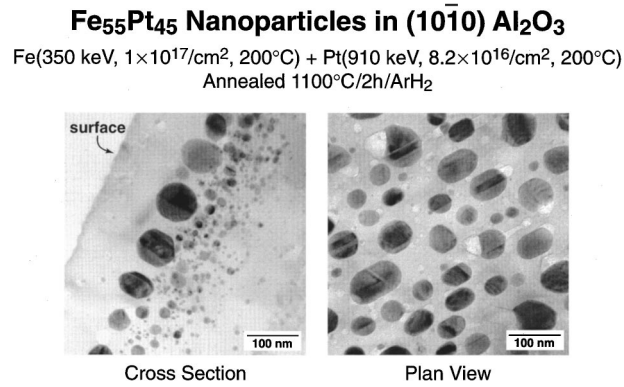

FIG. 15. Cross-section and plan-view TEM micrographs for $(10\bar{1}0)$ Al_2O_3 implanted by Fe (350 keV, $1\times10^{17}/cm^2$, 200 °C)+Pt (910 keV, $8.2\times10^{16}/cm^2$, 200 °C) followed by annealing (1100 °C/2 h/Ar +4% H_2).

the sample implanted to the higher dose (Fig. 9). The coercivity remains reasonable even at room temperature for these smaller nanoparticles.

Extremely high values of coercivity have been measured also using Al_2O_3 samples with different crystallographic orientations. One such result is shown in Fig. 14. Magnetization measurements (at 5 and 300 K) are shown in Fig. 14(a) for the case of *M*-plane-oriented $(10\bar{1}0)$ Al_2O_3 implanted and annealed under the same conditions as those appropriate to Figs. 7–9. At 5 K, the coercivity is approximately 34 kOe and remains in excess of 25 kOe even at room temperature—as shown in Fig. 14(b). Cross-section and plan-view micrographs showing the microstructure and particle size in the *M*-plane sample are illustrated in Fig. 15. The nanoparticles exhibit a bimodal size distribution with a band of large particles (maximum diameter of ~70 nm) located at a depth of ~145 nm. In addition, there is a high density of much smaller particles located at a somewhat greater depth. In plan view, the FePt nanoparticles are often associated with voids, and many of the nanoparticles have internal domains. The largest particle in plan view or cross section is ~85 nm, and there is no evidence for the threading network of particles observed in the *c*-axis sample (Fig. 8) even though the particles are quite large in the *M*-plane sample also. Extremely high values of coercivity have also been produced when *A*-plane $(11\bar{2}0)$ and *R*-plane $(10\bar{1}2)$ Al_2O_3 crystals were implanted and annealed under the same conditions as the samples corresponding to Figs. 8 and 15. It is likely that the microstructure in these Al_2O_3 crystals with the *A* and *R* orientation is similar to that observed in the *M*-plane sample (Fig. 15), but this remains to be confirmed by TEM observations.

C. Formation of Fe_3Pt and $FePt_3$ nanoparticles

Thus far, we have discussed the results obtained by ion-beam synthesis when nearly equal doses of Fe and Pt are used. By changing the relative ion doses substantially, we have synthesized nanoparticles of two other phases in the Fe-Pt system as expected from the Fe-Pt phase diagram.[32] Figure 16 shows the x-ray diffraction results for Al_2O_3 crystals implanted with Fe and Pt to give alloy compositions of $Fe_{74}Pt_{26}$ and $Fe_{27}Pt_{73}$. Both samples were annealed under the same conditions (1100 °C/2 h/Ar+4% H_2) to cause precipi-

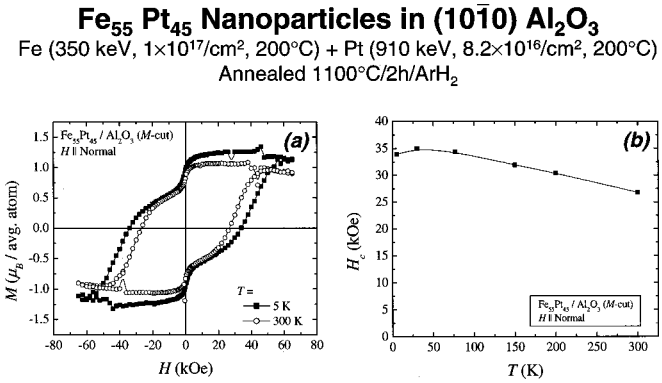

FIG. 14. Magnetic properties of *M*-cut Al_2O_3 implanted by Fe (350 keV, $1\times10^{17}/cm^2$, 200 °C)+Pt (910 keV, $8.2\times10^{16}/cm^2$, 200 °C) followed by annealing (1100 °C/2 h/Ar+4% H_2). Magnetization curves measured at $T=5$ and 300 K with *H* normal to the surface are shown in (a). The temperature dependence of the coercivity is shown in (b).

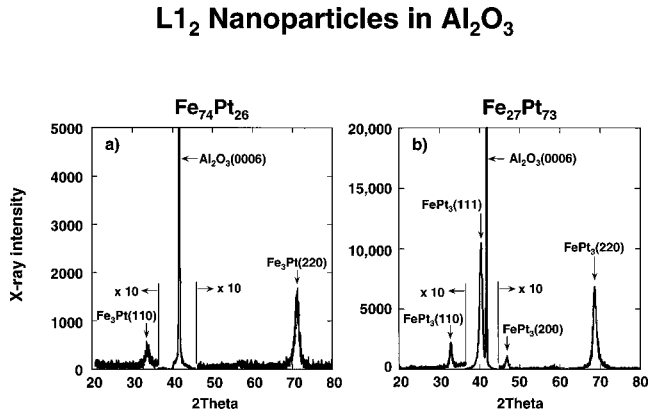

FIG. 16. X-ray diffraction results from *c*-axis-oriented Al_2O_3 crystals implanted by Fe and Pt in the alloy composition of (a) $Fe_{74}Pt_{26}$ and (b) $Fe_{27}Pt_{73}$. Ion doses for $Fe_{74}Pt_{26}$ were $\sim1\times10^{17}/cm^2$ for Fe and $\sim3.3\times10^{16}/cm^2$ for Pt. Ion doses for $Fe_{27}Pt_{73}$ were $\sim5\times10^{16}/cm^2$ for Fe and $\sim1.5\times10^{17}/cm^2$ for Pt. Fe was implanted at $T=550$ °C and Pt at $T=500$ °C.

Downloaded 11 Sep 2009 to 160.91.157.167. Redistribution subject to AIP license or copyright; see http://jap.aip.org/jap/copyright.jsp

tation and nanoparticle formation. In Fig. 16(a), the x-ray spectrum from the $Fe_{74}Pt_{26}$ sample is consistent with that expected from the ordered phase of fcc Fe_3Pt which has the $L1_2$ structure. Strong lines from both superlattice (110) and fundamental (220) reflections are seen, and a probable (111) Fe_3Pt reflection is obscured by the very intense Al_2O_3 (0006) reflection. Rocking-curve measurements through the (220) reflection show the nanoparticles to be oriented along the Al_2O_3 *c*-axis. From high-resolution θ-2θ scans through the (220) diffraction peak, the value determined for the lattice parameter is 3.742 Å, which is expanded (by 0.27%) compared with the value[33] of 3.732 Å for bulk Fe_3Pt. From integrated rocking-curve measurements, the integrated intensity ratio $I(110)/I(220)$ is $\sim 0.34 \pm 0.04$, which yields the order parameter $S = \sim 0.6$ [for (220)-oriented domains] using the results of Table I and Eq. (3).

In Fig. 16(b), the x-ray scan from the $Fe_{27}Pt_{73}$ sample is consistent with that expected from the ordered phase of $FePt_3$, which also has the $L1_2$ structure. Strong lines from superlattice (110) and fundamental (220) reflections are observed in the x-ray spectra in addition to a strong (111) $FePt_3$ reflection. The $FePt_3$ nanoparticles are oriented with respect to the Al_2O_3 *c*-axis as demonstrated by x-ray rocking-curve measurements. X-ray diffraction measurements show the nanoparticles have a cubic lattice parameter of 3.873 Å as determined from a high-resolution θ-2θ scan through the (111) reflection. This is expanded (by 0.18%) compared to the value[34] of 3.866 Å for bulk $FePt_3$. Some of the expansion might be due to incorporation of Al into the nanoparticles during precipitation. In addition, ordered alloys of the form[35,36] Pt_3Al have allowed diffraction peaks very near those observed in Fig. 16(b)—so a precise identification of $FePt_3$ is not possible, but it is likely that the nanoparticles formed are $FePt_3$ with some incorporation of Al. From the data of Fig. 16(b), the integrated intensity ratio $I(110)/I(220)$ is estimated to be ~ 0.21 which for $FePt_3$ implies that the order parameter S for the (220)-oriented domains is ~ 0.84. Incorporation of Al into the alloy would increase the predicted ratio and reduce the estimate of the order parameter. Therefore, from the x-ray diffraction measurements in Fig. 16, the (220)-oriented domains for both Fe_3Pt and $FePt_3$ show evidence for ordering although they are not as well ordered as the fct FePt nanoparticles with the $L1_0$ structure.

Cross-section TEM micrographs showing the microstructure and the particle size in the near surface for both $Fe_{74}Pt_{26}$ and $Fe_{27}Pt_{73}$ in Al_2O_3 are illustrated in Fig. 17. For $Fe_{74}Pt_{26}$, the maximum particle size is ~ 25 nm in diameter, and the particles are nearly spherical with evidence for faceting in some of the nanoparticles. For $Fe_{27}Pt_{73}$, the particle size is smaller, and the particle shape is more elliptical with the largest particles being ~ 20 nm along the major axis of the ellipse. Numerous $Fe_{27}Pt_{73}$ particles shown in Fig. 17 exhibit Moiré fringes.

The results presented in Figs. 16 and 17 show that it was possible to form oriented nanoparticles of Fe_3Pt and $FePt_3$ by ion-beam synthesis where the relative does of Fe and Pt were adjusted to produce the desired alloy composition. The ordered phase of Fe_3Pt, which has the Cu_3Au structure, is

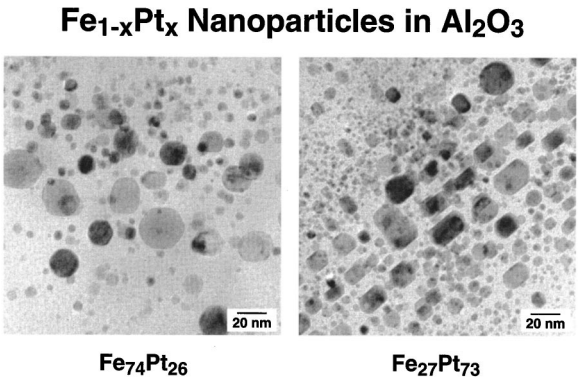

FIG. 17. Cross-section TEM micrographs for $Fe_{74}Pt_{26}$ (left) and $Fe_{27}Pt_{73}$ (right) nanoparticles in Al_2O_3. Ion doses in each case are the same as those given in Fig. 16.

known to exhibit giant magnetostriction[33] and is ferromagnetic with a Curie temperature of ~ 435 K.[37] This material has been prepared in single-crystal form by arc melting (see, for example, Refs. 33 and 37). It has also been produced in thin-film form by MBE (Ref. 38) or sputter deposition.[39] Fe_3Pt undergoes an order-disorder transition at a temperature of $\sim 840\,°C$. The sample in Fig. 16(a) was annealed above this temperature and then cooled slowly through the transition temperature following annealing. For these annealing conditions, the order parameter is considerably less than that measured for the $Fe_{55}Pt_{45}$ nanoparticles with the $L1_0$ structure. We have obtained preliminary results suggesting that the order parameter for Fe_3Pt can be improved somewhat (from $S \sim 0.6$ to $S \sim 0.7$) by a long anneal (700 °C/17 h) below the transition temperature, but additional work is required to optimize this annealing treatment.

The chemically ordered phase of $FePt_3$ has the Cu_3Au cubic $L1_2$ structure, and it is antiferromagnetic (with two different kinds of antiferromagnetic ordering) in the chemically ordered state.[40,41] The fcc chemically disordered phase, however, is ferromagnetic. Disorder can be introduced by a number of methods including mechanical deformation[40,42] as well as deviations from stoichiometry.[40,43] Films of $FePt_3$ have been produced by sputter deposition[39] and by MBE.[41] The $Fe_{27}Pt_{73}$ nanoparticles that we have produced by ion-beam synthesis have an order parameter less than unity, so some disorder exists in these nanoparticles, and there is a 2% deviation from ideal stoichiometry. The annealing temperature (1100 °C) is considerably below the order-disorder transition temperature ($\sim 1350\,°C$), so annealing at temperatures lower than 1100 °C should not be necessary to induce or improve order.

Magnetization curves measured for the samples containing $Fe_{74}Pt_{26}$ and $Fe_{27}Pt_{73}$ nanoparticles are shown in Fig. 18. The $Fe_{74}Pt_{26}$ sample is ferromagnetic but with a very low coercivity (~ 0.72 kOe at 5 K and ~ 0.25 kOe at 300 K). Both the saturation magnetization and the coercivity decrease as the temperature increases. [Results from this sample are included in the plot of H_c versus Pt atomic fraction shown in Fig. 6(b).] The magnetization curves for $Fe_{27}Pt_{73}$ in Fig. 18 show that the nanoparticles formed by ion implantation are ferromagnetic at 5 K with a coercivity of

Downloaded 11 Sep 2009 to 160.91.157.167. Redistribution subject to AIP license or copyright; see http://jap.aip.org/jap/copyright.jsp

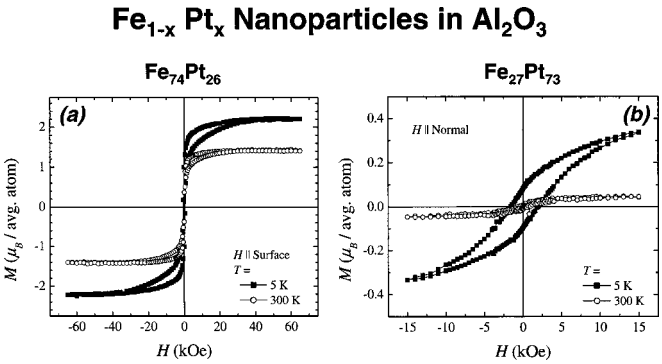

FIG. 18. Magnetization curves measured for $Fe_{74}Pt_{26}$ (a) and $Fe_{27}Pt_{73}$ (b) in Al_2O_3. Ion doses in each sample are the same as those given in Figs. 14–16. Magnetization curves were measured at $T=5$ and $T=300$ K with H parallel to the sample surface for the $Fe_{74}Pt_{26}$ sample and with H perpendicular to the surface for the $Fe_{27}Pt_{73}$ sample.

~2.0 kOe, but at room temperature, the coercivity and the saturation magnetization are very low. This ferromagnetic (rather than antiferromagnetic) behavior is attributed to the disorder in the nanoparticles or to a deviation from stoichiometry.

D. Implantation of Fe only or Pt only

Nanoparticles are also formed by the implantation of Fe or Pt alone into *c*-axis-oriented Al_2O_3 followed by annealing. X-ray diffraction results for Fe implanted into Al_2O_3 at several implantation temperatures followed by annealing are shown in Fig. 19. In the temperature range of implantation at room temperature to 200 °C, the nanoparticles formed are α-Fe with their $\langle 110 \rangle$ axis directed along the *c*-axis of the Al_2O_3 host single crystal. If the implantation is carried out at 550 °C, however, clear evidence for the formation of $FeAl_2O_4$ is observed (from the 220 reflection). Evidence for both Fe_2O_3 and α-Fe is observed in the sample implanted at liquid nitrogen temperature (LN_2). (Fe_2O_3 is believed to result from oxidation of Fe segregated to the surface during annealing when the sample is removed from the furnace.) In each case, nanoparticles are oriented along the *c* axis of the Al_2O_3 host.

X-ray diffraction results for the case of Pt implanted into Al_2O_3 at two temperatures followed by annealing are shown in Fig. 20, and this gives convincing evidence for the incorporation of Al into the Pt nanoparticles. Both spectra show evidence for fcc Pt nanoparticles oriented with their $\langle 111 \rangle$ axis parallel to the Al_2O_3 *c*-axis. However, in the sample implanted at 500 °C, the diffraction line at $2\theta \sim 32.8°$ cannot arise from fcc Pt, and we attribute this peak to the formation of an ordered alloy of the form Pt_nAl. A likely candidate[35,36] is Pt_3Al, which has diffraction lines close to those shown in Fig. 20. Therefore, the precipitates formed after the 500 °C annealing are believed to contain a fairly high concentration of Al atoms in addition to Pt. In the sample implanted at 200 °C, the fcc forbidden peaks are greatly reduced in intensity, and these nanoparticles are believed to contain substantially less incorporated Al. From the results shown in Fig. 20, it is clear that implantation at the higher temperature (500 °C) is required to form the ordered alloy Pt_nAl. This

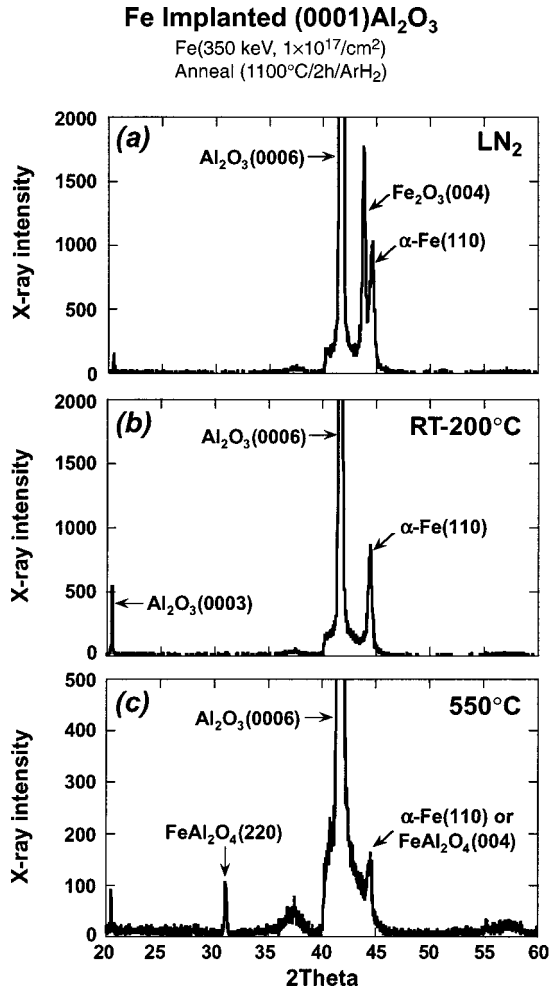

FIG. 19. X-ray diffraction results for Fe (350 keV, $1\times10^{17}/cm^2$) implanted into Al_2O_3 followed by annealing (1100 °C/2 h/Ar+4% H_2). Results are shown for implantation temperatures of (a) LN_2, (b) RT to 200 °C, and (c) 550 °C.

suggests that this phase nucleates during implantation at the higher temperature, with the nuclei growing during subsequent annealing.

Figure 21 shows the microstructure in the near-surface region for samples implanted by Fe or Pt at high temperature, followed by annealing. For the case of Fe, after annealing there is a high density of cavities or voids in the very near surface, followed by nanoparticles containing Fe at a somewhat greater depth. The Fe-containing precipitates have diameters up to ~65 nm. The Pt-containing nanoparticles have a cubic shape and are much smaller with maximum particle sizes up to ~12 nm on a side.

Magnetization measurements have also been made on the Al_2O_3 crystals implanted by Fe or Pt only and are shown in Fig. 5. For the case of Fe implantation at 500 °C, the nanoparticles are ferromagnetic with a coercivity of ~0.14 kOe. If the implantation is carried out at 200 °C, the resulting Fe nanoparticles have a coercivity of ~0.13 kOe, but the saturation magnetization is ~20% higher than for the sample implanted at 550 °C. The fact that the magnetic properties of the samples implanted at 550 and 200 °C are nearly the same provides evidence that most of the nanoparticles in the

Downloaded 11 Sep 2009 to 160.91.157.167. Redistribution subject to AIP license or copyright; see http://jap.aip.org/jap/copyright.jsp

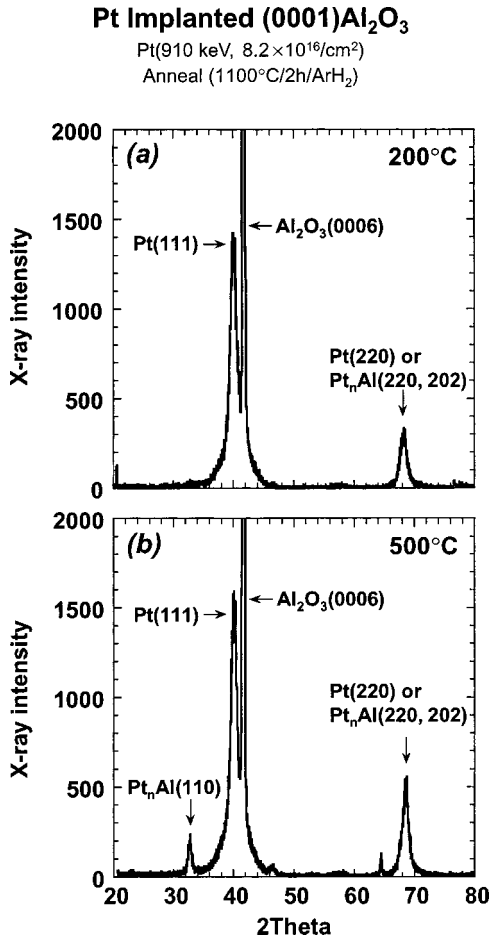

FIG. 20. X-ray diffraction results for Pt (910 keV, $8.2\times10^{16}/\mathrm{cm}^2$) implanted into Al_2O_3 followed by annealing (1100 °C/2 h/Ar+4% H_2). Results are shown for implantation temperatures of (a) 200 °C and (b) 500 °C.

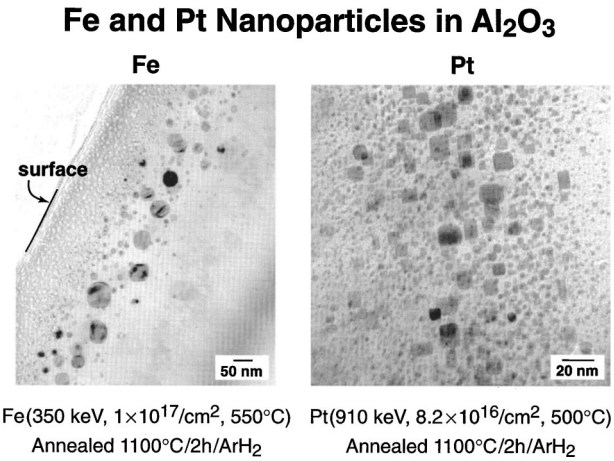

FIG. 21. Cross-section TEM micrographs showing Fe and Pt nanoparticles in Al_2O_3. Crystals were implanted by Fe (350 keV, $1\times10^{17}/\mathrm{cm}^2$, 550 °C) or Pt (910 keV, $8.2\times10^{16}/\mathrm{cm}^2$, 500 °C). Implanted crystals were annealed at 1100 °C/2 h/Ar+4% H_2.

sample implanted at 550 °C are α-Fe—even though the x-ray diffraction results (Fig. 19) suggest that a mixture of α-Fe and $FeAl_2O_4$ may be present. Others[44] have reported that $FeAl_2O_4$ is not ferromagnetic, and this may explain the 20% difference in the saturation magnetization for samples implanted at the different temperatures. For the case of Pt implanted into Al_2O_3 at 500 °C, Fig. 5 shows that both the saturation magnetization and the coercivity are nearly zero indicating that the Pt_nAl nanoparticles are not contributing to the magnetic properties of any of the $Fe_{1-x}Pt_x$ samples we have discussed.

The structural and/or magnetic properties of Al_2O_3 implanted by Fe at room temperature or near liquid nitrogen temperature have been investigated extensively in the past.[45–49] Implantation at elevated temperatures (240 °C) has also been investigated,[44,50] but to a lesser extent. These studies have shown that α-Fe nanoparticles are formed by annealing implanted Al_2O_3 in a reducing environment. The particles are oriented and can have sizes up to several tens of nanometers. When annealed in the range of 800–1200 °C in a reducing atmosphere or vacuum, the particles are ferromagnetic if the size exceeds the superparamagnetic limit (~5 nm in diameter), and coercivities of 0.1–0.3 kOe have been reported.[44,48–50] If samples implanted by Fe are annealed at 1450 °C, then diffraction lines from $FeAl_2O_4$ only were observed,[44] and this phase did not contribute to the magnetization of the sample. These prior results are consistent with those we have obtained.

The formation of coherent Pt precipitates in Al_2O_3 has also been observed by others[51] as a result of the implantation of Pt into *c*-axis-oriented Al_2O_3 at room temperature, followed by annealing in air. The average size of the Pt precipitates was estimated to be ~25 nm, which is larger than the precipitates we observe following high-temperature implantation and annealing in a reducing environment (maximum size of ~10 nm; see Fig. 21). In addition, no evidence for the formation of Pt_nAl was noted following the room temperature implantation. This is reasonable since our work suggests that the formation of Pt_nAl decreases as the implantation temperature decreases.

IV. CONCLUSIONS

$Fe_{1-x}Pt_x$ nanoparticles covering a wide range of alloy compositions have been formed in Al_2O_3 single crystals by ion-beam synthesis. In the range of Pt atomic fractions from $x\sim35\%$ to 55%, the chemically ordered tetragonal $L1_0$ structure of FePt is formed. These nanoparticles are ferromagnetic with extremely high magnetic coercivities. The coercivity is a strong function of Pt atomic fraction and reaches its maximum value (~22 kOe) for the slightly Fe-rich alloy composition $Fe_{55}Pt_{45}$ in *c*-axis-oriented Al_2O_3. The FePt nanoparticles formed in Al_2O_3 by ion-beam synthesis are crystallographically oriented with respect to the Al_2O_3 host matrix, but the orientation, particle size, and microstructure depend strongly on the implantation conditions. For implantation at high temperatures (550 °C for Fe and 500 °C for Pt), the FePt nanoparticles exhibit multiple orientations with respect to the *c* axis of Al_2O_3. These nanoparticles are nearly spherical and are in the size range of 2–10 nm with a few particles as large as 25 nm diameter (for doses of $\sim1\times10^{17}/\mathrm{cm}^2$ of each impurity). If the implantation is carried out at lower temperatures (200 °C for each impurity) to the same doses ($\sim1\times10^{17}/\mathrm{cm}^2$ of each impurity), then anneal-

Downloaded 11 Sep 2009 to 160.91.157.167. Redistribution subject to AIP license or copyright; see http://jap.aip.org/jap/copyright.jsp

ing gives rise to an interconnected network of very large particles (~50 nm thick). Some of these particles extend up to a size of ~2 μm parallel to the surface. These large particles have a single orientation [i.e., (111) FePt is parallel to (0001) Al_2O_3]. The formation of this interconnected network of large particles is correlated with the formation of a buried amorphous layer during implantation. Crystallization of the buried amorphous layer during annealing is believed to give rise to the formation of interconnected large particles. The magnetic coercivities associated with the large particles are ~23 kOe in *c*-axis Al_2O_3 and up to ~33 kOe for *M*-, *R*-, or *A*-plane Al_2O_3 (at 5 K).

For FePt nanoparticles formed by ion-beam synthesis in Al_2O_3, the measured order parameters are larger than would be expected for fully ordered FePt alloys, and this suggests that a lighter element such as Al is also incorporated into the alloy nanoparticles. Therefore, it is likely that the nanoparticles that we have formed are fully ordered but contain Al atoms in addition to Fe and Pt. The magnetic coercivities we have measured are among the highest ever observed for FePt films or nanoparticles prepared by any processing method. It is possible that this enhanced coercivity results from Al incorporated into the FePt nanoparticles, but further experiments are required to determine if this is, in fact, the case.

By changing the relative doses of Fe and Pt substantially, we have also formed $Fe_{74}Pt_{26}$ and $Fe_{27}Pt_{73}$ nanoparticles in Al_2O_3. X-ray diffraction measurements suggest that these particles correspond to the ordered $L1_2$ structure of cubic Fe_3Pt and $FePt_3$ respectively, but the order parameter for these nanoparticles is 0.5–0.8, indicating that some disorder remains in the nanoparticles. For the Fe-rich case ($Fe_{74}Pt_{26}$), the saturation magnetization is large and indicative of a well-developed ferromagnet. In contrast, the Pt-rich case ($Fe_{27}Pt_{73}$) has a much lower saturation magnetization reflecting the possibility of both antiferro- and ferromagnetic ordering near this composition. For both cases, the magnetic coercivity is lower. Finally, we have synthesized oriented Fe and Pt nanoparticles in *c*-axis-oriented Al_2O_3. The Fe nanoparticles are ferromagnetic with a coercivity of ~0.14 kOe while the Pt nanoparticles are nonmagnetic. Clear evidence has been obtained for the formation of oriented $FeAl_2O_4$ and Pt_nAl nanoparticles in samples that were implanted by Fe or Pt alone at the high implantation temperatures. This demonstrates that impurities from the substrate can be incorporated into the nanoparticles if implantation is carried out at high temperatures.

It should also be noted that FePt nanoparticles with high coercivity can be formed in other substrates. We have formed FePt nanoparticles with magnetic coercivities exceeding 30 kOe by ion implantation into SiO_2 matrices.[13] In addition, we have demonstrated that CoPt nanoparticles with coercivities exceeding 10 kOe can be formed in Al_2O_3 by ion implantation and annealing. These results are reported in a separate publication.[52]

ACKNOWLEDGMENTS

We thank Darrell Thomas and Dale Hensley for their monumental efforts in helping with all of the implants required for this work. We thank J. Tischler for use of his program for calculating diffraction intensities from thin films. Part of this research was sponsored by the Laboratory Directed Research and Development Program of Oak Ridge National Laboratory. Oak Ridge National Laboratory is managed by UT-Battelle, LLC, for the U.S. Department of Energy under Contract No. DE-AC05-00OR22725.

[1] D. Weller, A. Moser, L. Folks, M. E. Best, W. Lee, M. F. Toney, M. Schwickert, J.-U. Thiele, and M. F. Doerner, IEEE Trans. Magn. **36**, 10 (2000).
[2] K. Inomata, T. Sawa, and S. Hashimoto, J. Appl. Phys. **64**, 2537 (1988).
[3] S. Sun, C. B. Murray, D. Weller, L. Folks, and A. Moser, Science **287**, 1989 (2000). See also IEEE Trans. Magn. **37**, 1239 (2001).
[4] R. F. C. Farrow, D. Weller, R. F. Marks, M. F. Toney, D. J. Smith, and M. R. McCartney, J. Appl. Phys. **84**, 934 (1998).
[5] M. R. Visokay and R. Sinclair, Appl. Phys. Lett. **66**, 1692 (1995).
[6] B. M. Lairson, M. R. Visokay, R. Sinclair, and B. M. Clemens, Appl. Phys. Lett. **62**, 639 (1993).
[7] D. Ravelosona, C. Chappert, V. Mathet, and H. Bernas, Appl. Phys. Lett. **76**, 236 (2000).
[8] M. Watanabe, T. Masumoto, D. H. Ping, and K. Hono, Appl. Phys. Lett. **76**, 3971 (2000).
[9] B. Bian, D. Laughlin, K. Sato, and Y. Hirotsu, J. Appl. Phys. **87**, 6962 (2000).
[10] C. P. Luo and D. J. Sellmyer, Appl. Phys. Lett. **75**, 3162 (1999).
[11] C. P. Luo, S. H. Liou, L. Gao, Y. Liu, and D. J. Sellmyer, Appl. Phys. Lett. **77**, 2225 (2000).
[12] C.-M. Kuo and P. C. Kuo, J. Appl. Phys. **87**, 419 (2000).
[13] C. W. White, S. P. Withrow, J. D. Budai, L. A. Boatner, K. D. Sorge, J. R. Thompson, K. S. Beaty, and A. Meldrum, Nucl. Instrum. Methods Phys. Res. B **191**, 437 (2002).
[14] JCPDS—International Center for Diffraction Data, Powder Diffraction File #43-1359 (ICDD, Newton Square, PA, 1997).
[15] B. E. Warren, *X-Ray Diffraction* (Addison-Wesley, Reading, MA, 1969), Chap. 12.
[16] A. Cebollada, D. Weller, J. Sticht, G. R. Harp, R. F. C. Farrow, R. F. Marks, R. Savoy, and J. C. Scott, Phys. Rev. B **50**, 3419 (1994).
[17] T. Shima, T. Moriguchi, S. Mitani, and T. Takanashi, Appl. Phys. Lett. **80**, 288 (2002).
[18] A. Z. Men'shikov, Yu. A. Dorofeyev, V. A. Kazantsev, and S. K. Sidorov, Phys. Met. Metallogr. **38**(3), 47 (1974).
[19] J. P. Liu, Y. Liu, C. P. Luo, Z. S. Shan, and D. J. Sellmyer, J. Appl. Phys. **81**, 5644 (1997).
[20] J. P. Liu, C. P. Luo, Y. Liu, and D. J. Sellmyer, Appl. Phys. Lett. **72**, 483 (1998).
[21] I. Panagiotopoulos, S. Stavroyiannis, D. Niachos, J. A. Christodoulides, and G. C. Hadjipanayis, J. Appl. Phys. **87**, 4358 (2000).
[22] T. Goto, Y. Ide, H. Abe, K. Watanabe, J. Onagawa, H. Yoshida, and J. M. Cadogan, J. Magn. Magn. Mater. **198–199**, 486 (1999).
[23] E. E. Fullerton, D. T. Margulies, M. E. Schabes, M. Carey, B. Gurney, A. Moser, M. Best, G. Zeltzer, K. Rubin, H. Rosen, and M. Doerner, Appl. Phys. Lett. **77**, 3806 (2000).
[24] H. Zeng, S. Sun, T. S. Vadantam, J. P. Liu, Z. R. Dai, and Z. L. Wang, Appl. Phys. Lett. **89**, 2583 (2002).
[25] T. Maeda, T. Kai, A. Kikitsu, T. Nagase, and J. Akiyama, Appl. Phys. Lett. **80**, 2147 (2002).
[26] O. Kitakami, Y. Shimada, K. Oikawa, H. Daimon, and K. Fukamichi, Appl. Phys. Lett. **78**, 1104 (2001).
[27] D. H. Ping, M. Ohnuma, K. Hono, M. Watanabe, T. Iwasa, and T. Masumoto, J. Appl. Phys. **90**, 4708 (2001).
[28] C. W. White, C. J. McHargue, P. S. Sklad, L. A. Boatner, and G. C. Farlow, Mater. Sci. Rep. **4**, 41 (1989).
[29] P. S. Sklad, J. C. McCallum, C. J. McHargue, and C. W. White, Nucl. Instrum. Methods Phys. Res. B **46**, 102 (1990).
[30] N. Yu, P. C. McIntyre, M. Nastasi, and K. E. Sickafus, Phys. Rev. B **52**, 17518 (1995).
[31] J. D. Budai, C. W. White, S. P. Withrow, M. F. Chisholm, J. Zhu, and R. A. Zuhr, Nature (London) **390**, 384 (1997).
[32] *Binary Alloy Phase Diagrams, Volume 1*, edited by T. B. Massalski (American Society for Metals, Metals Park, Ohio, 1986).

Downloaded 11 Sep 2009 to 160.91.157.167. Redistribution subject to AIP license or copyright; see http://jap.aip.org/jap/copyright.jsp

[33] T. Kakeshita, T. Takeuchi, T. Fukuda, M. Tsujiguchi, T. Saburi, R. Oshima, and S. Muto, Appl. Phys. Lett. **77**, 1502 (2000).
[34] JCPDS—International Center for Diffraction Data, Powder Diffraction File #29-0716 (ICDD, Newton Square, PA, 2000).
[35] JCPDS—International Center for Diffraction Data, Powder Diffraction File #29-0070 (ICDD, Newton Square, PA, 2000).
[36] JCPDS—International Center for Diffraction Data, Powder Diffraction File #48-1670 (ICDD, Newton Square, PA, 1997).
[37] T. Sasaki and S. Chikazumi, J. Phys. Soc. Jpn. **46**, 1732 (1979).
[38] Y. M. Hu, J. C. A. Huang, S. Y. Huang, and T. H. Wu, IEEE Trans. Magn. **37**, 2417 (2001).
[39] S. W. Yung, Y. H. Chang, T. J. Lin, and M. P. Huang, J. Magn. Magn. Mater. **116**, 411 (1992).
[40] G. E. Bacon and J. Crangle, Proc. R. Soc. London, Ser. A **272**, 387 (1963).
[41] S. Maat, O. Hellwig, G. Zeltzer, E. E. Fullerton, G. J. Mankey, M. L. Crow, and J. L. Robertson, Phys. Rev. B **63**, 134426 (2001).
[42] S. Takahashi and Y. Umakoshi, J. Phys.: Condens. Matter **2**, 2133 (1990).
[43] D. Palaith, C. W. Kimball, R. S. Preston, and J. Crangle, Phys. Rev. **178**, 795 (1969).
[44] M. Ohkubo, T. Hioki, and J. Kawamoto, J. Appl. Phys. **62**, 3069 (1987).
[45] C. J. McHargue, P. S. Sklad, C. W. White, G. C. Farlow, A. Perez, and G. Maest, J. Mater. Res. **6**, 2145 (1991).
[46] C. J. McHargue, P. S. Sklad, C. W. White, J. C. McCallum, A. Perez, and G. Marest, J. Mater. Res. **6**, 2160 (1991).
[47] C. J. McHargue, S. X. Ren, P. S. Sklad, L. F. Allard, and J. Hunn, Nucl. Instrum. Methods Phys. Res. B **116**, 173 (1996).
[48] H.-G. Jang, H.-B. Kim, J.-H. Joo, C.-N. Whang, H.-K. Kim, D.-W. Moon, J. J. Woo, and S.-O. Kim, Nucl. Instrum. Methods Phys. Res. B **124**, 528 (1997).
[49] E. Alves, C. J. McHargue, R. C. Silva, C. Jesus, O. Conde, M. F. da Silva, and J. C. Soares, Surf. Coat. Technol. **128–129**, 434 (2000).
[50] M. Ohkubo, T. Hioki, N. Suzuki, T. Ishiguro, and J. Kawamoto, Nucl. Instrum. Methods Phys. Res. B **39**, 675 (1989).
[51] E. Alves, R. C. da Silva, O. Conde, M. F. da Silva, and J. C. Soares, Nucl. Instrum. Methods Phys. Res. B **148**, 1049 (1999).
[52] S. P. Withrow, C. W. White, J. D. Budai, L. A. Boatner, K. D. Sorge, J. R. Thompson, and R. Kalyanaraman, J. Magn. Magn. Mater. **260**, 319 (2003).

Downloaded 11 Sep 2009 to 160.91.157.167. Redistribution subject to AIP license or copyright; see http://jap.aip.org/jap/copyright.jsp